ACS APPLIED ENERGY MATERIALS

www.acsaem.org Article

2D-Nb_2CT_z-Supported, 3D-Carbon-Encapsulated, Oxygen-Deficient Nb_2O_5 for an Advanced Li-Ion Battery

Junfeng Huang, Teng Sun, Meiyi Ma, Zhong Xu, Yuchen Wang, Yanting Xie, Xiang Chu, Xinglin Jiang, Yongbin Wang, Shenglong Wang, Weiqing Yang, and Haitao Zhang*

Cite This: https://doi.org/10.1021/acsaem.1c03680 Read Online

ACCESS | Metrics & More | Article Recommendations | Supporting Information

ABSTRACT: Exploring advanced electrode materials with rapid lithium-ion charging/discharging kinetic properties is significant for the development of modern electric transportation. Herein we report a powerful synergistic engineering of carbon encapsulation and oxygen deficiency to construct Nb_2O_5 through a two-step method of pregelation and annealing treatment. The yielded Nb_2O_5 with sufficient oxygen vacancies are supported by 2D highly conductive Nb_2CT_z (T = O, OH, and F) MXene and further encapsulated by 3D carbon layers (2D/3D Nb_2O_{5-x}). Such an exquisite architecture is proved to efficiently overcome the intrinsic weakness of slow ion transfer, low electrical conductivity, and long-term cycling instability in metal oxides, in this case Nb_2O_5. Consequently, 2D/3D Nb_2O_{5-x} composites share an improved average diffusion coefficient from 1.34×10^{-12} cm^{-2} s^{-1} to 3.02×10^{-12} cm^{-2} s^{-1}, a facilitated Li^+ ion diffusion pathway, and shortened relaxation time constant (τ_0) from 8.9 to 6.1 ms. In an optimized 2D/3D Nb_2O_{5-x} electrode, it delivers a high capacity of 245 mAh g^{-1} at 0.1 C (1 C = 270 mA g^{-1}), 85 mAh g^{-1} at a high rate of 5 C, and an excellent long-term durability with 92.7% capacity retention during 1250 cycles. These results clearly demonstrate the significance of tailoring the microstructure and composition of metal oxides as used in high-rate and long-cycling lithium-ion storage.

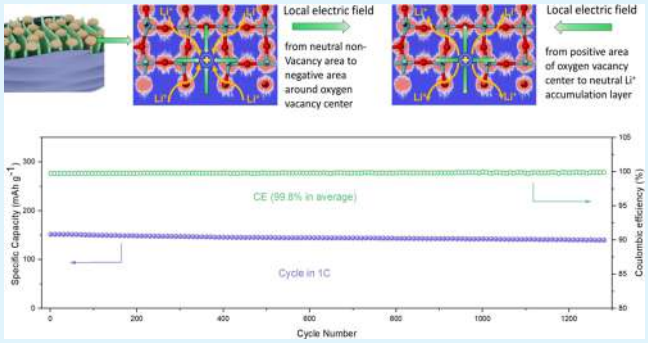

KEYWORDS: *Nb_2O_5, Nb_2C MXene, 2D/3D hierarchical structure, oxygen vacancy, carbon encapsulation*

INTRODUCTION

With the rapid growth of fossil energy consumption in industry, transportation, and energy supply, large quantities of harmful gases and carbon dioxide release into the atmosphere, causing air contamination and global warming, which has presented a challenge to sustainable development.[1] To meet future energy demands and reduce carbon dioxide emissions, China has proposed to peak carbon dioxide emissions before 2030 and achieve carbon neutrality before 2060.[2] As one of the most promising environmentally friendly energy storage devices, Li-ion batteries (LIBs) have already attracted global attention.[3] As for anodes, commercial graphite has reached the theoretical upper limit of specific capacity which puts sand on the wheel of its application in electric vehicles.[4] Therefore, state-of-the-art LIBs can only be created when excellent alternative anodes with high specific capacity and energy are explored. Metal oxides with high capacity and energy are identified as viable alternative anodes.[5] However, they still suffer from some apparent drawbacks, such as poor electrical conductivity, slow ion transfer, and long-term cycling instability,[6] which extremely impede their development in LIB anodes. Therefore, it is urgent to solve the above-mentioned issues of metal oxides.

Currently, a large body of research has been conducted to promote rate and cycle properties. Among them, the most representative one is the construction of nanomaterials with enlarged surface area and abundant active sites to accelerate the transfer of Li ions and electrons via shortening the diffusion path.[7−10] However, since most battery electrodes are inherently low in conductivity, it is still challenging to make electrode materials perform well with this strategy alone. In such a context, vacancy engineering as an alternative strategy has also been frequently used in both bulk and nanostructured electrodes to accelerate electron/Li-ion transport, stabilize the structure, and improve the surface functionalization.[11] Typically, the designed oxygen vacancies in metal oxides promote the electron/Li-ion transfer through a synergistic effect of activating the tetrahedral in the Li ion and inducing the local built-in electric field.[12−16] To be specific, enough

Received: November 22, 2021
Accepted: January 18, 2022

Downloaded via SOUTHWEST JIAOTONG UNIV on February 24, 2022 at 03:30:57 (UTC).
See https://pubs.acs.org/sharingguidelines for options on how to legitimately share published articles.

oxygen vacancies, located in the bandgap of metal oxides, introduce a shallow electron donor and therefore provide an accordingly narrow bandgap that is efficient for high electrical conductivity and rapid self-recovery capacity. For example, an abundant oxygen-deficient Co_3O_4 mesoporous nanostructure showed a modulated conductive behavior from semiconductivity to metallicity.[17] Meanwhile, oxygen vacancies in Li-sulfur battery electrodes helped improve the adsorption of lithium polysulfides (LiPSs) and hence inhibited their shuttle effect.[18,19] These pioneering works guide boosting the properties of electrode materials through a method of constructing defect engineering for advanced electrochemical energy storage.

It should be noted that the above-discussed strategies still cannot solve the long-term cycling instability of metal oxide anodes. Hence, an additional carbon coating technology is commonly incorporated to withstand mechanical deformation and enhance electronic conductivity. This coated carbon layer, grown by chemical vapor deposition (CVD),[20,21] hydrothermicity,[22] electrodeposition,[23] or atomic layer deposition (ALD),[24] was proved to efficiently elevate long-term cycling stability. For example, the Nb_2O_5 was usually encapsulated by carbon to perform as a stabilized anode.[25−27] Besides, the manufacture of $MnFe_2O_4$@C nanofibers via an electrospinning approach showed excellent cycling performance.[28] Given all that, taking full advantage of nanostructuring, oxygen vacancies, and carbon-coating techniques can achieve the goal of killing three birds with one stone.

In this study, a two-step method of pregelation and annealing treatment is put forward to construct 2D-Nb_2CT_z-supported, 3D-carbon-encapsulated, and oxygen-deficient Nb_2O_5 (named 2D/3D Nb_2O_{5-x}) LIB anode materials. We demonstrate that Nb_2O_{5-x} materials in situ grow on 2D Nb_2CT_z nanosheets and simultaneously 3D carbon layers yielded from pyrolysis of gelatinizer-encapsulated 2D Nb_2CT_z@Nb_2O_{5-x} composites. The construction of oxygen vacancy engineering and 3D carbon encapsulation is proved to effectively boost the Li-ion diffusion coefficient, rate performance, and structural stability. As a result, the rationally designed 2D/3D Nb_2O_{5-x} anodes possess high specific capacity (245 mAh g^{-1} at 0.1 C), large rate capability (85 mAh g^{-1} at 5 C), and extremely long-term cycling stability (92.7% capacity retention over 1250 cycles at 1 C).

■ EXPERIMENTAL SECTION

Preparation of Nb_2CT_z MXene Materials. The Nb_2CT_z MXene was prepared by a modified solution etching method with LiF and HCl as the etching agents. The Nb_2AlC MAX powders were purchased from 11 Technology (Jilin, China) and used as the raw materials. First, 2.0 g of LiF was dissolved into 30 mL of HCl (9 M) under continuous stirring for 10 min, followed by careful addition of 1.2 g of Nb_2AlC powders. The Nb_2AlC MAX phase was etched at various times (24−120 h) at 55 or 70 °C. After that, the obtained colloidal solutions were washed with deionized water and centrifuged several times until the pH of the solution reached 6. Finally, the as-prepared Nb_2CT_z powders were collected via vacuum filtration and further dried at 40 °C overnight.

Preparation of Nb_2CT_z Gels. Nb_2CT_z water suspension (marked as solution A) with a concentration of 30 mg mL^{-1} was prepared by intense ultrasonication, and different concentrations of *k*-carrageenan (5−20 mg mL^{-1}) were prepared through stirring in deionized water for 1 h at 80 °C (marked as solution B) to explore the proper conditions. Then, solution A and solution B with a volume ratio of 1:1 were mixed together and further stirred at 40 °C for about 1 h to obtain a homogeneous colloidal solution. We also discussed the effect of different types of cross-linking agents on the quality of Nb_2CT_x-based hydrogels and aerogels. Next, the formed colloidal solution was thoroughly freeze-dried to prepare the Nb_2CT_z and *k*-carrageenan composite aerogels.

Preparation of 2D/3D Nb_2O_{5-x}. For synthesizing 2D/3D Nb_2O_{5-x} composites, the optimized Nb_2CT_z and *k*-carrageenan aerogels were further heat-treated. The samples were annealed at a relatively high temperature of 600 °C by adjusting the annealing time from 6 to 36 h under the protection of Ar/H_2 gas with a flow rate of 80 sccm and then naturally cooled to room temperature. The prepared samples were named 2D/3D Nb_2O_{5-x}-6, 2D/3D Nb_2O_{5-x}-12, 2D/3D Nb_2O_{5-x}-18, 2D/3D Nb_2O_{5-x}-24, 2D/3D Nb_2O_{5-x}-30, and 2D/3D Nb_2O_{5-x}-36 according to the annealing time. For comparison, Nb_2CT_z without pregelation treatment was directly annealed at 600 °C for 24 h, and the obtained sample was named Nb_2CT_z-24.

Characterization Methods. X-ray diffraction (XRD) patterns were obtained with a PANlytical X'Pert powder diffractometer. JEOL JEM-2100 F transmission electron microscopy (TEM) was used to characterize the morphologies and defects of the samples. Scanning electron microscopy (SEM) and X-ray energy-dispersive spectroscopy (EDX, JSM-7800F Prime) were used for morphology detection and elemental mapping analysis. The Raman spectrum was conducted on an RM2000 microscopic confocal Raman spectrometer employing a 532 nm laser beam. The X-ray photoelectron spectroscopy (XPS) depth profile was recorded with a Thermo Scientific ESCALAB 250Xi spectrometer. To characterize the oxygen vacancies of 2D/3D Nb_2O_{5-x}, electron paramagnetic resonance (EPR) spectra were recorded on a JEOL JES-FA200. The Brunauer−Emmett−Teller (BET) surface area and pore size distribution were determined by nitrogen adsorption and desorption using a Micrometritics ASAP2460 analyzer.

Computing Method. The theoretical calculations were performed by density functional theory (DFT) implemented in the Cambridge Sequential Total Energy Package (CASTEP).[29] The Perdew−Burke−Ernzerhof (PBE) exchange-correlation function of the generalized gradient approximation (GGA) was employed for calculation, and the ultrasoft pseudopotential was chosen for the ion−electron interactions whereby pseudo atomic calculation was performed for O $2s^22p^4$ and Nd $4s^24p^64d^45s^1$. After single-point energy optimization, an energy cutoff of 420 eV was chosen to allow the energy and the force convergence until 1×10^{-5} eV and 0.03 eV/Å. Brillouin zone sampling of the Nb_2O_5 and Nb_2O_{5-x} units was carried out with 5 × 5 × 1 meshes using the Monkhorst−Pack method for geometry optimization, and a denser mesh of 7 × 7 × 2 was used for computing the electron density differences and electron localization function of the Nb_2O_5 and Nb_2O_{5-x}. To consider the strong correlation effect of 3d transition metal (TM) atoms, the GGA plus Hubbard *U* (GGA + *U*) method is used to calculate the structural relaxation and electronic properties, and an effective U_{eff} ($U - J$) = 2.0 eV of the Nb TM atoms is used.

Electrochemical Measurements. The active material was mixed with Super P (Timical, Switzerland) and polyvinylidene fluoride solution (Arkema, France, 4.0 wt % in *N*-methyl pyrrolidone solution) at a weight ratio of 8:1:1 in a moderate amount of *N*-methyl pyrrolidone to obtain electrode slurry. Then, the slurry was coated on a copper foil (9 μm). The as-obtained electrodes were dried in a vacuum oven at 120 °C for 24 h to remove the solvents. The mass loading of the active material is 2.2−3.1 mg cm^{-2}. The electrochemical performance of the 2D/3D Nb_2O_{5-x} electrodes was evaluated using CR2032 coin-type cells with Li metal as the counter/reference electrode. A Neware battery testing system (Neware, China) was used to evaluate the rate and cycling performance of cells with the measured voltage ranging from 0.05 to 2.5 V. Cyclic voltammetry curves and electrochemical impedance spectra were carried out using the electrochemical workstation (CHI660E, China). For galvanostatic intermittent titration technique (GITT) measurement, the coin-type cells were first charged or discharged at a constant current pulse of 0.1 C for 30 min, followed by an equal duration relaxation of 10 h, allowing the equilibrium

https://doi.org/10.1021/acsaem.1c03680
ACS Appl. Energy Mater. XXXX, XXX, XXX−XXX

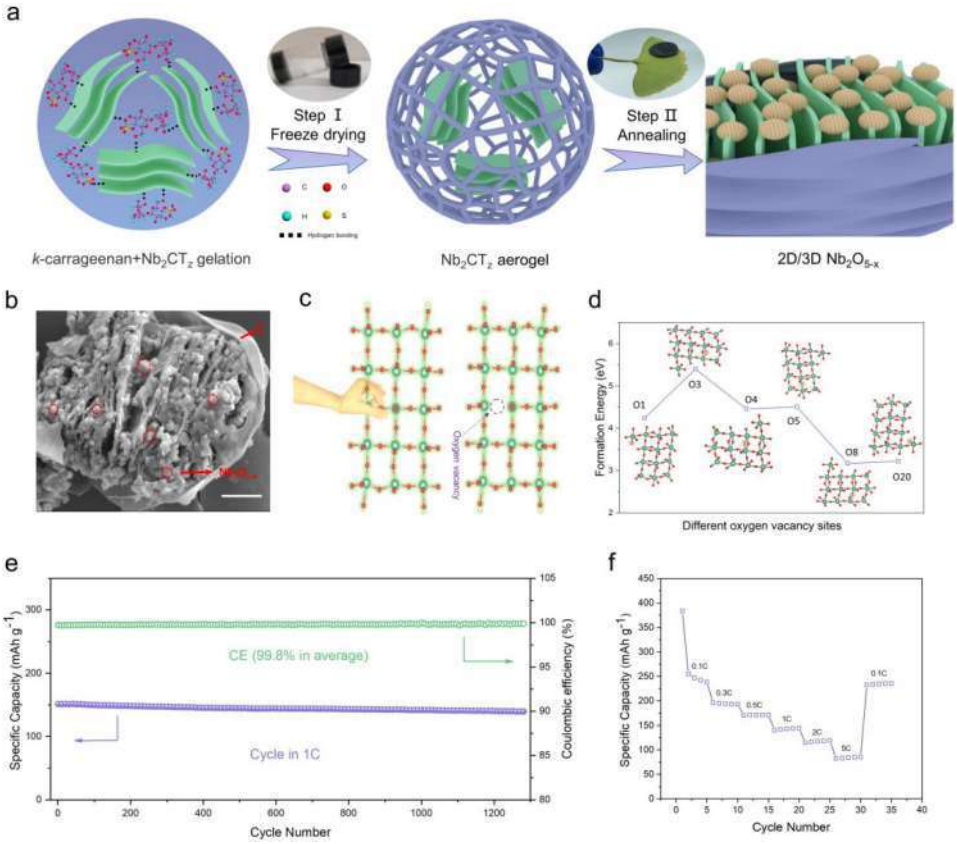

Figure 1. Designed 2D/3D Nb_2O_{5-x}. (a) Schematically illustrating a two-step method of pregelation and annealing treatment to construct 2D/3D Nb_2O_{5-x}. (b) Representative SEM images of 2D/3D Nb_2O_{5-x}. (c) Construction of oxygen defects via an annealing treatment. (d) DFT-calculated formation energy of oxygen vacancies at different lattice sites. (e) Long-term cyclic stability and Coulombic efficiency of 2D/3D Nb_2O_{5-x} after 1250 cycles at a current rate of 1 C. (f) Gravimetric capacity at different current densities as a function of the discharge rate. Scale bar (b): 1 μm.

potential of lithium storage at different points to be probed in the whole voltage window.

■ RESULTS AND DISCUSSION

To explore the optimal etching technology of Nb_2AlC, different etching measures and times have been discussed. As shown in X-ray diffraction (XRD) patterns (Supporting Information Figure S1a), HF etching agents with a concentration of 50% yield low mass production of Nb_2CT_z MXenes and cause a security threat at 55 °C for 40 h. Hence, an optimized etching process of LiF + HCl with different time was chosen to prepare Nb_2CT_z MXene. With the increase of etching time, the characteristic peak of Nb_2CT_z located at around 6.8° becomes increasingly apparent, manifesting higher mass production of Nb_2CT_z MXene. After successful etching (Supporting Information Figure S1b), Nb_2CT_z MXene shows a representative laminated construction like an accordion (Supporting Information Figure S1c−f) and is functionalized by some O and F terminations (Supporting Information Figure S1g−j).

The as-prepared Nb_2CT_z MXene can form homogeneous hydrogels and aerogels under the gelation action of *k*-carrageenan (Figure 1a). We discussed the effect of different types of cross-linking agents on the quality of Nb_2CT_z-based hydrogels (Supporting Information Figure S2a−d). The results obviously indicated that only *k*-carrageenan and gelatin could form glorious hydrogels. Since *k*-carrageenan promoted the formation of densified hydrogels, indicated by a much smaller volume (Supporting Information Figure S2d), it was chosen to be a cross-linking agent. At this point, hydrogels with different shapes could be perfectly formed (Supporting Information Figure S3a) and well restored after intensive extrusion (Supporting Information Figure S3b−d). The aerogels duplicate these characteristics under the process of vacuum freeze-drying as shown in step I of Figure 1a. SEM images show an apparent 3D network structure of Nb_2CT_z-based aerogels (Supporting Information Figure S4).

As the Nb_2CT_z@*k*-carrageenan aerogels were subjected to annealing in an Ar/H_2 atmosphere with a H_2 ratio of 6.0 vol %, two effects were simultaneously stimulated such that the already cross-linked *k*-carrageenan was carbonized, and Nb_2CT_z was partially oxidized. The directly grown carbon materials encapsulated onto the surface of Nb_2CT_z nanosheets and in situ formed Nb-based oxides gave rise to oxygen vacancies at H_2 containing reductive conditions. Eventually, novel 2D-Nb_2CT_z-supported, 3D-carbon-encapsulated, and oxygen-deficient Nb_2O_{5-x} (2D/3D Nb_2O_{5-x}) materials came into being, as shown in step II of Figure 1a.

The representative SEM images of 2D/3D Nb_2O_{5-x} are displayed in Figure 1b and Supporting Information Figure S5a−f, in which the Nb_2CT_z MXene nanosheet shows a complete and obvious 2D-layered structure. Some spherical Nb_2O_{5-x} particles with oxygen vacancies grow on the layered structure and uniformly distribute on the surface of Nb_2CT_z because of its high specific surface area and reactivity.[30,31] In experiment, H_2 gas at high temperature (like 600 °C) shares the strong reducibility and acts as a scissor to capture oxygen atoms in the Nb-based oxides. The produced −OH radicals

https://doi.org/10.1021/acsaem.1c03680
ACS Appl. Energy Mater. XXXX, XXX, XXX−XXX

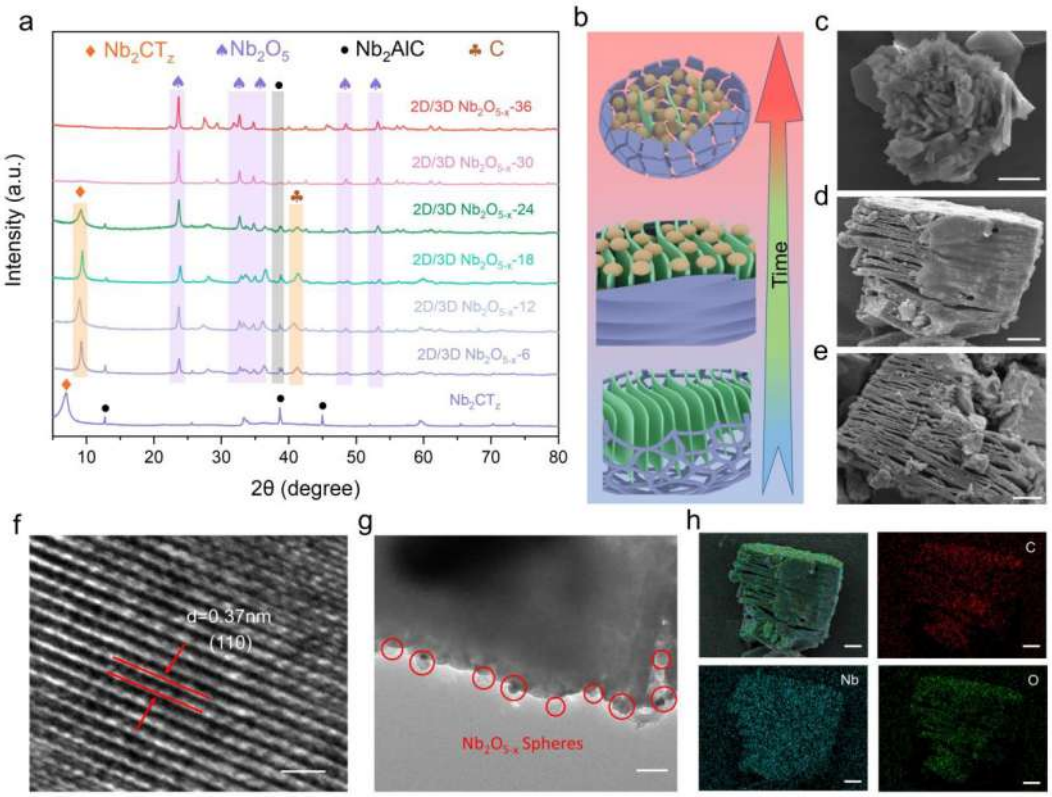

Figure 2. Compositions and structures of 2D/3D Nb_2CT_z@Nb_2O_{5-x}. (a) XRD patterns of Nb_2CT_z and its aerogels prepared at different annealing times. (b) Schematically showing the evolution of 2D/3D synergetic structure with increasing annealing times. SEM images of (c) 2D/3D Nb_2O_{5-x}-36, (d) 2D/3D Nb_2O_{5-x}-24, and (e) Nb_2CT_z. (f) HRTEM image of 2D/3D Nb_2O_{5-x}-24 indicates the (110) lattice spacing of Nb_2O_5. (g) TEM image of 2D/3D Nb_2O_{5-x}-24. (h) EDS elemental mapping images of Nb, C, and O in the 2D/3D Nb_2O_{5-x}-24 composite. Scale bars: c−e, h, 1 μm; f, 1 nm; and g, 100 nm.

that are unstable in nature subsequently react with H atoms to form H_2O molecules and then desorb, which is irreversible and hence leads to oxygen defects (Figure 1c).[32] In theory, Nb_2O_5 materials are inclined to form oxygen vacancies, which is illustrated by the relatively low oxygen-defect formation energy (Figure 1d). The formation energy for oxygen vacancies at different lattice sites ranges from 3.2 to 5.4 eV, indicating a stable crystal structure of Nb_2O_{5-x} after introducing oxygen vacancies.

By optimizing the kinetic behavior and alleviating the volume expansion through hierarchical 2D/3D structural design and defect engineering, 2D/3D Nb_2O_{5-x} electrodes exhibit extremely stable circulation (92.7%@1250 cycles) at the 1 C rate with an average Coulombic efficiency (CE) up to 99.8% and deliver a discharge capacity of 245 mAh g^{-1} (0.1 C rate).

We systematically investigated the effect of annealing time on the microstructure and compositions of 2D/3D Nb_2O_{5-x}. The pristine Nb_2CT_z shows a strong diffraction peak at 6.8° assigned to the (002) plane of Nb_2CT_z MXene (Figure 2a). Consistent with the XRD results, the pristine Nb_2CT_z possesses a typically stratified structure (Figure 2b and 2e). As the annealing time increases, the peak of Nb_2CT_z shifts to the higher 2θ degree because of the reduced electrostatic repulsion and accumulation of MXene nanosheets that originated from the interaction between H_2 gas and Nb_2CT_z.[33−37] Meanwhile, the peaks of Nb_2O_5 and carbon materials located at 23.6°, 32.2°, 34.7°, 48.2°, 53.1°, and 41.7°, respectively, have come out gradually. With prolonging annealing time, one main diffraction peak intensity of (110) at 23.6° becomes stronger and stronger, implying increasingly higher content of Nb_2O_5 in 2D/3D Nb_2O_{5-x}. However, too long annealing time leads to the collapse of Nb_2CT_z MXene as shown in Figure 2b and 2c. The progress of carbonization in a moderate degree results in well-retained MXene nanosheets and in situ growth of Nb_2O_{5-x} nanoparticles (Figure 2b−e and Supporting Information Figure S6a−e), while the excessive annealing treatment causes undesired oxidization and breaks the structural balance. Therefore, it can be concluded that the target structure (2D/3D Nb_2O_{5-x}) can only be obtained under appropriate annealing time (like 21 h or 24 h).

Raman spectra also confirm the existence of Nb_2O_5 and a carbon-coating layer (Supporting Information Figure S7). Meanwhile, HRTEM characterization confirms that the 2D/3D Nb_2O_{5-x}-24 sample possesses a high degree of crystallization. The marked lattice fringe with a distance of 0.37 nm belongs to the (110) crystal plane of Nb_2O_5 (Figure 2f). As illustrated in Figure 2g, the compositions of 2D/3D Nb_2O_{5-x}-24 are dominated by MXene lamella and Nb_2O_5 spherical particles (the area circled in the diagram). There is also a darker area on the top of the nanosheet, implying the presence of a carbon-encapsulating layer. The uniformity of 2D/3D Nb_2O_{5-x}-24 is also verified by EDS mapping. The elements of Nb, O, and C homogeneously distribute in the 2D/3D Nb_2O_{5-x}-24 sample. In short, 2D Nb_2CT_z and 3D-carbon-encapsulated supported Nb_2O_{5-x} nanoparticles were successfully prepared.

https://doi.org/10.1021/acsaem.1c03680
ACS Appl. Energy Mater. XXXX, XXX, XXX−XXX

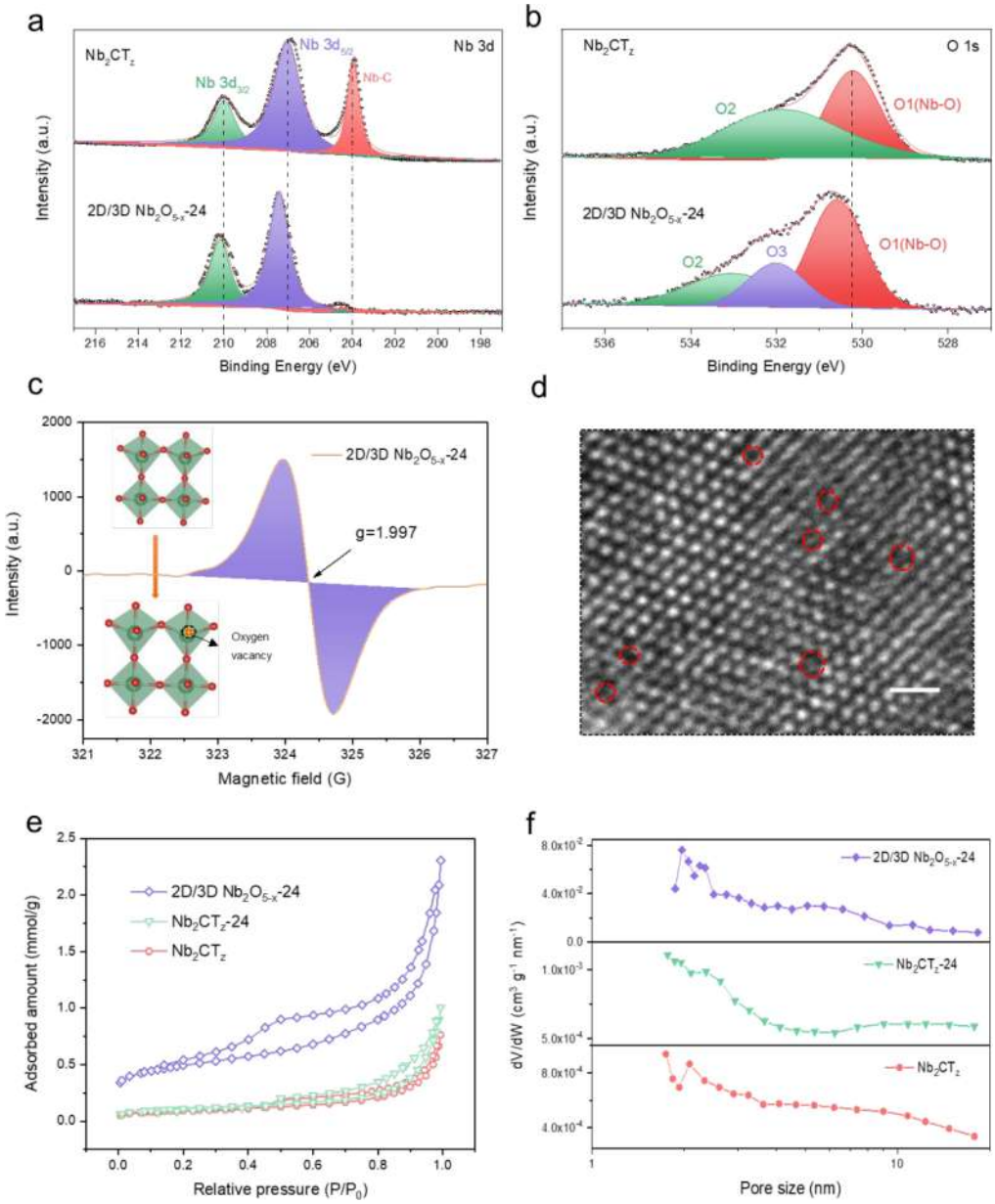

Figure 3. Demonstration of oxygen vacancies. (a) Nb 3d XPS spectra of Nb_2CT_z and 2D/3D Nb_2O_{5-x}-24. (b) O 1s XPS spectra of Nb_2CT_z and 2D/3D Nb_2O_{5-x}-24. (c) EPR pattern of 2D/3D Nb_2O_{5-x}-24. (d) HRTEM image of 2D/3D Nb_2O_{5-x}-24. (e) Nitrogen adsorption−desorption isotherm of Nb_2CT_z, Nb_2CT_z-24 and 2D/3D Nb_2O_{5-x}-24. (f) Pore size distribution of Nb_2CT_z, Nb_2CT_z-24 and 2D/3D Nb_2O_{5-x}-24. Scale bar: d, 1 nm.

We further prove that the synthesized Nb_2O_5 nanoparticles are in an oxygen-deficient state. Deconvoluted XPS spectra of Nb 3d in Nb_2CT_z MXene (Figure 3a) display three obvious characteristic peaks located at 210.0, 207.0, and 203.9 eV, representing Nb $3d_{3/2}$, Nb $3d_{5/2}$, and Nb−C peaks, respectively. As in 2D/3D Nb_2O_{5-x}-24, these three peaks shift to higher binding energy (BE), corresponding to the increment of the Nb valence state after annealing treatment of Nb_2CT_z. Meanwhile, the intensity of the Nb−C peak has decreased sharply after 24 h annealing treatment due to the superficial transition of Nb_2CT_z into Nb_2O_{5-x}. High-resolution O 1s spectra of Nb_2CT_z also exhibit two sub peaks (O1, O2) located at 530.2 and 531.8 eV, which correspond to the Nb−O bond and hydroxylated surface.[38] In contrast, the O1 peak becomes much stronger and shifts up to a higher BE region for 2D/3D Nb_2O_{5-x}-24, suggesting the structural transformation of Nb_2CT_z into Nb_2O_{5-x}. Moreover, an additional O3 peak appears at 532.0 eV, apparently indicating the formation of oxygen defects.[39]

Furthermore, EPR is a direct and progressive measure to detect oxygen vacancies of materials. It provides a finger printing of unpaired electrons of the nanomaterial, a signal for oxygen vacancies. EPR tests of 2D/3D Nb_2O_{5-x}-24 show a strong EPR signal at g = 1.997, confirming a large proportion of oxygen vacancies in 2D/3D Nb_2O_{5-x},[19] as illustrated in Figure 3c. We further used HRTEM characterization to detect the structural defects of 2D/3D Nb_2O_{5-x}, and the results were shown in Figure 3d. In HRTEM images, the bright spots represent the atomic configuration of Nb_2O_5, while some dark holes marked by red dotted circles indicate the presence of oxygen vacancies. Besides, the nitrogen adsorption−desorption isotherms have been conducted to investigate the surface

https://doi.org/10.1021/acsaem.1c03680
ACS Appl. Energy Mater. XXXX, XXX, XXX−XXX

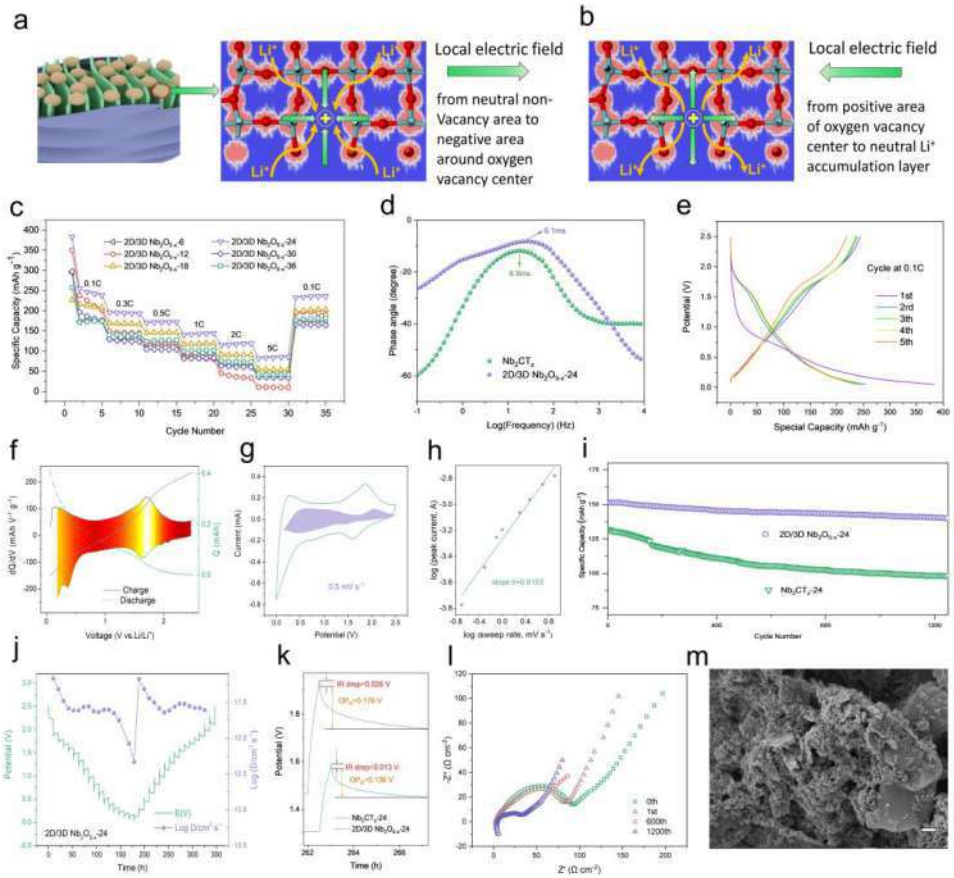

Figure 4. LIBs based on 2D/3D Nb_2O_{5-x} electrodes. (a) Schematically showing the imbalanced charge distribution around the oxygen vacancy, alleviating Li^+ transport during discharging. (b) Discharging process. (c) Gravimetric capacity at different current densities as a function of the discharge rate for different annealing times. (d) Relaxation time for Nb_2CT_z and 2D/3D Nb_2O_{5-x}-24. (e) The discharge/charge curves of 2D/3D Nb_2O_{5-x}-24 cycling at 0.1 C. (f) dQ/dV plot for 2D/3D Nb_2O_{5-x}-24. (g) The CV curve of 2D/3D Nb_2O_{5-x}-24 at 0.5 mV s^{-1}. (h) log(i) versus log(ν) at different scan rates. (i) Long-term cyclic stability of 2D/3D Nb_2O_{5-x}-24 and UA-24 after 1250 cycles at a current rate of 1 C. (j) GITT results for 2D/3D Nb_2O_{5-x}-24. (k) GITT local magnified image for 2D/3D Nb_2O_{5-x}-24 and Nb_2CT_x-24. (l) EIS plots of 2D/3D Nb_2O_{5-x}-24 for 0, 1, 600, and 1200 cycles. (m) SEM images of the 2D/3D Nb_2O_{5-x}-24 electrode. Scale bars: m, 1 μm.

physical parameters. As shown in Figure 3e, the Brunauer–Emmett–Teller (BET) surface area of 2D/3D Nb_2O_{5-x} is 39.6 m^2 g^{-1}, which is much higher than that of Nb_2CT_z (7.6 m^2 g^{-1}) and Nb_2CT_z-24 (8.5 m^2 g^{-1}). The increment of specific surface area is probably ascribed to the introduction of a carbon layer and oxygen vacancies. As shown in Figure 3f, 2D/3D Nb_2O_{5-x} possesses two apparent peaks of mesoporous size distributions (1.97 and 2.23 nm), which is beneficial to promote the penetration of the electrolyte ions.

To gain insight into the synergistic effect of 2D/3D architecture design and oxygen vacancies, we systematically investigate the electrical and electrochemical properties of 2D/3D Nb_2O_{5-x}. First, the electron localization function (ELF) around oxygen vacancies was calculated by DFT computation. After the formation of an oxygen vacancy (O8), the ELF has become much more disordered (Supporting Information Figure S8). Moreover, the electron distribution around the oxygen vacancy exhibits lower electron density, which is quite different from the symmetrical defect-free sites. The lopsided charge distribution around the vacancies will result in an in-plane built-in electric field, which may boost Li^+ transport by providing an extra Coulomb force.[40−42] Specifically, the lower electron density endows the central zone of oxygen vacancies positively charged, while the zone around oxygen vacancies is negatively charged (Figure 4a). Therefore, the electric field from the vacancy-free area to a negatively charged area around oxygen vacancies will offer a Coulombic attractive force to pin Li^+ ions like a lock-in effect during the lithiation process. As a consequence, the negatively charged area around oxygen vacancies will transform to electrical neutrality. In the subsequent delithiation process, the reverse electric field from the oxygen vacancy center to the neutral zone will promote the transport of Li^+ ions as well (Figure 4b).

The rate capability of various 2D/3D Nb_2O_{5-x} electrodes is exhibited in Figure 4c. Different annealing time leads to different structures and hence different rate properties. After annealing at only 6 h, the remaining original porous aerogel structure was beneficial to ion transport, leading to fair rate performance. As the annealing time reached 12 h, the original porous structure was greatly damaged, while nonconductive k-carrageenan was incompletely carbonized, causing inferior rate capability. With the increase of annealing time to 18−24 h, the structure has a preferable C-encapsulated Nb_2CT_z@Nb_2O_{5-x} structure containing an oxygen vacancy, showing good rate performance. As for 2D/3D Nb_2O_{5-x}-24, the specific capacity reaches up to 245 mAh g^{-1} at 0.1 C. When cycled at a high rate of 1, 2, and 5 C, still 143, 118, and 85 mAh g^{-1} can be maintained. With further increase of annealing time to 36 h, the structure of MXene was completely collapsed, resulting in declined rate performance instead. Supporting Information

https://doi.org/10.1021/acsaem.1c03680
ACS Appl. Energy Mater. XXXX, XXX, XXX−XXX

Figure S9 exhibits a 2D/3D Nb_2O_{5-x}-24 electrode with the smallest charge-transfer resistance (R_{ct} = 80 Ω), demonstrating its rapid charge-transfer process. Consistent with the BET results (Figure 3e, 3f), 2D/3D Nb_2O_{5-x}-24 has the higher surface area and proper mesopores that can shorten the ion transport path. The relaxation time constant (τ_0), determined from the EIS spectra, is another parameter to evaluate the rate capability. It is known that short relaxation time indicates fast frequency response of the device.[43,44] According to the equation of $\tau_0 = 1/(2\pi f)$, the τ_0 values are calculated to be 8.9 and 6.1 ms for Nb_2CT_z and 2D/3D Nb_2O_{5-x}-24, respectively (Figure 4d). The lower τ_0 value of 2D/3D Nb_2O_{5-x}-24 reveals its better rate capability, proving the positive effect of oxygen vacancy engineering and carbon encapsulation on Li-ion migration. The enhanced rate capability and decreased internal resistance of 2D/3D Nb_2O_{5-x}-24 are also shown in the Supporting Information Figure S10.

Although 2D/3D Nb_2O_{5-x}-24 has the best rate performance, its initial Coulombic efficiency is not the highest (Supporting Information Figure S11). The initial Coulomb efficiency of Nb_2CT_z, 2D/3D Nb_2O_{5-x}-12, Nb_2O_{5-x}-24, and Nb_2O_{5-x}-36 are 70.2%, 65.1%, 63.7%, and 60.2%, respectively. The relatively declined Coulombic efficiency of 2D/3D Nb_2O_{5-x}-24 in comparison with Nb_2CT_z may be ascribed to two aspects. First, with the insertion of Li^+ ions, the electrodes with some defect sites will absorb additional lithium ions to lower the system energy, leading to the irreversible capacity and accordingly low initial Coulombic efficiency. The second is that higher specific surface area of 2D/3D Nb_2O_{5-x}-24 will consume more irreversible Li^+ ions for the formation of a solid−electrolyte interphase (SEI) film.

Differential capacity versus voltage of 2D/3D Nb_2O_{5-x}-24 was conducted to further analyze the electrochemical properties (Figure 4f). During the charging process, a small voltage variation at 1.7 V results in a huge capacity change due to the electrochemical reaction, namely, the extraction of Li^+ ions. Meanwhile, there is a process of Li^+-ion insertion as the discharge voltage reaches 1.6 V, consistent with the CV results (Figure 4g). The CV curves at multiple scan rates from 0.2 to 5 mV s^{-1} are displayed in Supporting Information Figure S12. The separation of a Faradaic peak becomes apparent with the increase of scan rate from 0.2 to 5 mV s^{-1}, implying minimal polarization at a high rate. To explore the intrinsic electrochemical behavior, log(i) versus log(v) shown in Figure 4h yields a slope b value of ∼0.62, indicating both Li^+ ion intercalation and surface capacity. The increased surface capacity will facilitate good rate performance.[45] Actually, in 2D/3D Nb_2O_{5-x}-24, the capacitive effects increase from 24.8% to 60.1% as the scan rates increases from 0.2 to 5 mV s^{-1} (Figure 4g and Supporting Information Figure S13). Therefore, the high contribution of capacitive charge storage is attributed to large specific surface area and oxygen defects that promote sufficient electrochemical Li^+-ion intercalation and deintercalation as well as Li^+ ions stored at cluster gaps or interstitial sites.

Besides, long-term cycling performance of 2D/3D Nb_2O_{5-x}-24 at 1 C is shown in Figure 4i. Remarkably, an exceptionally long lifetime of 1250 cycles is achieved with a stable capacity of 140 mAh g^{-1} (92.7% of the pristine capacity), significantly higher than that of Nb_2CT_z-24. To gain insights into the dynamic behavior, we conducted GITT measurement for them. The IR drop of Nb_2O_{5-x}-24 is 0.013 V, and in Nb_2CT_x-24 it is double. Meanwhile, the diffusion overpotential (OP_D) of Nb_2CT_x-24 (0.176 V) is also higher than that of 2D/3D Nb_2O_{5-x}-24 (0.136 V) (Figure 4j,k and Supporting Information Figure S14). Moreover, the diffusion coefficient of 2D/3D Nb_2O_{5-x}-24 (1.34×10^{-12} cm^{-2} s^{-1}) is more than twice that of Nb_2CT_z-24 (3.02×10^{-12} cm^{-2} s^{-1}). Since the diffusion overpotential and diffusion coefficient are closely related to the transport dynamics of Li^+ ions through electrodes, we can conclude that 2D/3D Nb_2O_{5-x} possesses excellent ion and electron conductivity (Supporting Information Figure S15a) and high-rate long-cycling stability. In fact, the specific capacity of the Nb_2CT_z electrode is 27% lower than that of 2D/3D Nb_2O_{5-x}-24 after 1200 cycles at 1 C (Supporting Information Figure S15b).

Aiming at revealing the reason behind long-term cycling stability, we further performed EIS (Figure 4l) and SEM (Figure 4m and Supporting Information Figure S16) characterizations for pristine and cycled 2D/3D Nb_2O_{5-x}-24 electrodes. The uncirculated battery exhibits a high resistance (91 Ω) because of its relatively long diffusion path at the initial stage. However, after several lithium intercalation and deintercalation cycles, lithium ions can more easily transport between the layers due to the decreased diffusion path and enlarged layer spacing. After the first intercalation and deintercalation, the impedance is reduced to 84 Ω. As the cycles increase further to 600, the resistance decreases sharply to 35 Ω. After another 600 cycles, the R_{ct} does not change much, indicating the formation of a stable structure with low impedance.[46] As vividly shown in the Supporting Information Figure S16, untreated MXene has been completely pulverized, while 2D/3D Nb_2O_{5-x}-24 still possesses a typical nanosheet structure (Figure 4m) after 1000 cycles. This phenomenon is ascribed to the encapsulated 3D carbon which alleviates the structural variation, and the oxygen vacancy induced in situ electric field homogenizes the distribution of current density. The excellent cycling stability and high-rate capability of 2D/3D Nb_2O_{5-x}-24 indicate its potential application for electrochemical energy storage.

■ CONCLUSION

In summary, we have systematically investigated the synergistic effect of 2D Nb_2CTz support, 3D carbon encapsulation, and oxygen vacancy design on Li-ion storage capabilities for Nb_2O_5. We verified that proper annealing treatment was efficient to optimize Li-ion conduction behavior and material structural stability. The controlled introduction of oxygen vacancies in the nanosheet in turn affects the electronic structure of MXene. Consequently, a high reversible Li-ion capacity and good rate capability are delivered in 2D/3D Nb_2O_{5-x}. Charge distribution calculations of different oxygen-deficient Nb_2O_5 support an in-plane built-in electric field that is capable of offering an extra Coulomb force to promote Li^+ ion transfer. Our combined experimental and theoretical findings disclosing hierarchical 2D/3D design and oxygen defect engineering in metal oxides pave the way for a high-rate and long-cycling Li-ion battery.

■ ASSOCIATED CONTENT

Supporting Information

The Supporting Information is available free of charge at https://pubs.acs.org/doi/10.1021/acsaem.1c03680.

Figures S1−S16 that include additional results (PDF)

https://doi.org/10.1021/acsaem.1c03680
ACS Appl. Energy Mater. XXXX, XXX, XXX−XXX

AUTHOR INFORMATION

Corresponding Author

Haitao Zhang − *Key Laboratory of Advanced Technologies of Materials, Ministry of Education, School of Materials Science and Engineering, Southwest Jiaotong University, Chengdu 610031, China*; orcid.org/0000-0002-2057-7654; Email: haitaozhang@swjtu.edu.cn

Authors

Junfeng Huang − *Key Laboratory of Advanced Technologies of Materials, Ministry of Education, School of Materials Science and Engineering, Southwest Jiaotong University, Chengdu 610031, China*

Teng Sun − *Key Laboratory of Advanced Technologies of Materials, Ministry of Education, School of Materials Science and Engineering, Southwest Jiaotong University, Chengdu 610031, China*

Meiyi Ma − *Key Laboratory of Advanced Technologies of Materials, Ministry of Education, School of Materials Science and Engineering, Southwest Jiaotong University, Chengdu 610031, China*

Zhong Xu − *Key Laboratory of Advanced Technologies of Materials, Ministry of Education, School of Materials Science and Engineering, Southwest Jiaotong University, Chengdu 610031, China*

Yuchen Wang − *Key Laboratory of Advanced Technologies of Materials, Ministry of Education, School of Materials Science and Engineering, Southwest Jiaotong University, Chengdu 610031, China*

Yanting Xie − *Key Laboratory of Advanced Technologies of Materials, Ministry of Education, School of Materials Science and Engineering, Southwest Jiaotong University, Chengdu 610031, China*

Xiang Chu − *Key Laboratory of Advanced Technologies of Materials, Ministry of Education, School of Materials Science and Engineering, Southwest Jiaotong University, Chengdu 610031, China*

Xinglin Jiang − *Key Laboratory of Advanced Technologies of Materials, Ministry of Education, School of Materials Science and Engineering, Southwest Jiaotong University, Chengdu 610031, China*

Yongbin Wang − *Key Laboratory of Advanced Technologies of Materials, Ministry of Education, School of Materials Science and Engineering, Southwest Jiaotong University, Chengdu 610031, China*

Shenglong Wang − *Key Laboratory of Advanced Technologies of Materials, Ministry of Education, School of Materials Science and Engineering, Southwest Jiaotong University, Chengdu 610031, China*

Weiqing Yang − *Key Laboratory of Advanced Technologies of Materials, Ministry of Education, School of Materials Science and Engineering, Southwest Jiaotong University, Chengdu 610031, China*; orcid.org/0000-0001-8828-9862

Complete contact information is available at: https://pubs.acs.org/10.1021/acsaem.1c03680

Author Contributions

H.T.Z. conceptualized the work and supervised the research reported in the study. H.T.Z. and J.F.H. developed the methodology and conducted all experiments reported in this study. T.S., M.Y.M., Z.X., Y.C.W., Y.T.X., and J.X.L. performed the electrochemical performance characterizations. J.F.H. wrote the original draft. H.T.Z. further wrote and revised the manuscript. H.T.Z. and W.Q.Y. acquired funding for the work. All the authors approved the final version of the manuscript.

Notes

The authors declare no competing financial interest.

ACKNOWLEDGMENTS

We would like to thank the Analytical and Testing Center of Southwest Jiaotong University for their assistance with the TEM, SEM, XRD, and BET measurements. H.T.Z. and W.Q.Y. gratefully acknowledge the financial support from the National Natural Science Foundation of China (Nos. 51977185 and 51972277). H.T.Z. gratefully acknowledges the financial support from the Sichuan Science and Technology Program (No. 20ZDYF2833) and Southwest Jiaotong University Science and Technology Rising Star Program (No. 2682021CG021).

REFERENCES

(1) Wu, F.; Maier, J.; Yu, Y. Guidelines and trends for next-generation rechargeable lithium and lithium-ion batteries. *Chem. Soc. Rev.* **2020**, *49*, 1569−1614.

(2) Rogelj, J.; Huppmann, D.; Krey, V.; Riahi, K.; Clarke, L.; Gidden, M.; Nicholls, Z.; Meinshausen, M. A new scenario logic for the Paris Agreement long-term temperature goal. *Nature* **2019**, *573*, 357−363.

(3) Xu, Z.; Yang, T.; Chu, X.; Su, H.; Wang, Z.; Chen, N.; Gu, B.; Zhang, H.; Deng, W.; Zhang, H.; Yang, W. Strong lewis acid-base and weak hydrogen bond synergistically enhancing ionic conductivity of poly (ethylene oxide)@SiO_2 electrolytes for a high rate capability Li-metal battery. *ACS Appl. Mater. Interfaces* **2020**, *12*, 10341−10349.

(4) He, M.; Guo, R.; Hobold, G. M.; Gao, H.; Gallant, B. M. The intrinsic behavior of lithium fluoride in solid electrolyte interphases on lithium. *P. Natl. Acad. Sci. USA* **2020**, *117*, 73−79.

(5) Fang, S.; Bresser, D.; Passerini, S. Transition metal oxide anodes for electrochemical energy storage in lithium- and sodium-ion Batteries. *Adv. Energy Mater.* **2020**, *10*, 1902485.

(6) Wu, H. B.; Chen, J. S.; Hng, H. H.; Lou, X. W. Nanostructured metal oxide-based materials as advanced anodes for lithium-ion batteries. *Nanoscale* **2012**, *4*, 2526−2542.

(7) Cheng, X. B.; Zhang, R.; Zhao, C. Z.; Zhang, Q. Toward safe lithium metal anode in rechargeable batteries: a review. *Chem. Rev.* **2017**, *117*, 10403−10473.

(8) Deng, S.; Chao, D.; Zhong, Y.; Zeng, Y.; Yao, Z.; Zhan, J.; Wang, Y.; Wang, X.; Lu, X.; Xia, X.; Tu, J. Vertical graphene/$Ti_2Nb_{10}O_{29}$/hydrogen molybdenum bronze composite arrays for enhanced lithium ion storage. *Energy Storage Mater.* **2018**, *12*, 137−144.

(9) Li, H.; Shen, L.; Pang, G.; Fang, S.; Luo, H.; Yang, K.; Zhang, X. $TiNb_2O_7$ nanoparticles assembled into hierarchical microspheres as high-rate capability and long-cycle-life anode materials for lithium ion batteries. *Nanoscale* **2015**, *7*, 619−624.

(10) Hu, L.; Chen, Q. Hollow/porous nanostructures derived from nanoscale metal-organic frameworks towards high performance anodes for lithium-ion batteries. *Nanoscale* **2014**, *6*, 1236−1257.

(11) Qiao, Z.; Lin, L.; Yan, X.; Guo, W.; Chen, Q.; Xie, Q.; Han, X.; Lin, J.; Wang, L.; Peng, D. L. Function and application of defect chemistry in high-capacity electrode materials for Li-based batteries. *Chem. Asian J.* **2020**, *15*, 3620−3636.

(12) Qiu, B.; Zhang, M.; Wu, L.; Wang, J.; Xia, Y.; Qian, D.; Liu, H.; Hy, S.; Chen, Y.; An, K.; Zhu, Y.; Liu, Z.; Meng, Y. S. Gas-solid interfacial modification of oxygen activity in layered oxide cathodes for lithium-ion batteries. *Nat. Commun.* **2016**, *7*, 12108.

(13) Liu, T.; Dai, A.; Lu, J.; Yuan, Y.; Xiao, Y.; Yu, L.; Li, M.; Gim, J.; Ma, L.; Liu, J.; Zhan, C.; Li, L.; Zheng, J.; Ren, Y.; Wu, T.; Shahbazian-Yassar, R.; Wen, J.; Pan, F.; Amine, K. Correlation between manganese dissolution and dynamic phase stability in spinel-based lithium-ion battery. *Nat. Commun.* **2019**, *10*, 4721.

(14) Lin, T.; Schulli, T. U.; Hu, Y.; Zhu, X.; Gu, Q.; Luo, B.; Cowie, B.; Wang, L. Faster activation and slower capacity/voltage fading: a bifunctional urea treatment on lithium-rich cathode materials. *Adv. Funct. Mater.* **2020**, *30*, 1909192.

(15) Jing, P.; Liu, K.; Soule, L.; Wang, J.; Li, T.; Zhao, B.; Liu, M. Engineering the architecture and oxygen deficiency of T-Nb_2O_5-carbon-graphene composite for high-rate lithium-ion batteries. *Nano Energy* **2021**, *89*, 106398.

(16) Li, N.; Lan, X.; Wang, L.; Jiang, Y.; Guo, S.; Li, Y.; Hu, X. Precisely tunable T-Nb_2O_5 nanotubes via atomic layer deposition for fast-charging lithium-ion batteries. *ACS Appl. Mater. Interfaces* **2021**, *13*, 16445−16453.

(17) Sun, H.; Zhao, Y.; Molhave, K.; Zhang, M.; Zhang, J. Simultaneous modulation of surface composition, oxygen vacancies and assembly in hierarchical Co_3O_4 mesoporous nanostructures for lithium storage and electrocatalytic oxygen evolution. *Nanoscale* **2017**, *9*, 14431−14441.

(18) Li, Z.; Zhou, C.; Hua, J.; Hong, X.; Sun, C.; Li, H. W.; Xu, X.; Mai, L. Engineering oxygen vacancies in a polysulfide-blocking layer with enhanced catalytic ability. *Adv. Mater.* **2020**, *32*, 1907444.

(19) Luo, D.; Li, G.; Deng, Y. P.; Zhang, Z.; Li, J.; Liang, R.; Li, M.; Jiang, Y.; Zhang, W.; Liu, Y.; Lei, W.; Yu, A.; Chen, Z. Synergistic engineering of defects and architecture in binary metal chalcogenide toward fast and reliable lithium−sulfur batteries. *Adv. Energy Mater.* **2019**, *9*, 1900228.

(20) Liu, Y.; Liu, J.; Wang, J.; Banis, M. N.; Xiao, B.; Lushington, A.; Xiao, W.; Li, R.; Sham, T. K.; Liang, G.; Sun, X. Formation of size-dependent and conductive phase on lithium iron phosphate during carbon coating. *Nat. Commun.* **2018**, *9*, 929.

(21) Wang, J.; Yang, J.; Tang, Y.; Liu, J.; Zhang, Y.; Liang, G.; Gauthier, M.; Chen-Wiegart, Y. C.; et al. Size-dependent surface phase change of lithium iron phosphate during carbon coating. *Nat. Commun.* **2014**, *5*, 3415.

(22) Xie, D.; Xia, X.; Zhong, Y.; Wang, Y.; Wang, D.; Wang, X.; Tu, J. Exploring advanced sandwiched arrays by vertical graphene and N-doped carbon for enhanced sodium storage. *Adv. Energy Mater.* **2017**, *7*, 1601804.

(23) Shen, S.; Guo, W.; Xie, D.; Wang, Y.; Deng, S.; Zhong, Y.; Wang, X.; Xia, X.; Tu, J. A synergistic vertical graphene skeleton and S−C shell to construct high-performance $TiNb_2O_7$-based core/shell arrays. *J. Mater. Chem. A* **2018**, *6*, 20195−20204.

(24) Wan, G.; Yang, L.; Shi, S.; Tang, Y.; Xu, X.; Wang, G. $Ti_2Nb_{10}O_{29}$ microspheres coated with ultrathin N-doped carbon layers by atomic layer deposition for enhanced lithium storage. *Chem. Commun.* **2019**, *55*, 517−520.

(25) Lim, E.; Kim, H.; Jo, C.; Chun, J.; Ku, K.; Kim, S.; Lee, H. I.; Nam, I.-S.; Yoon, S.; Kang, K.; Lee, J. Advanced hybrid supercapacitor based on a mesoporous niobium pentoxide/carbon as high-performance anode. *ACS Nano* **2014**, *8*, 8968−8978.

(26) Lim, E.; Jo, C.; Kim, H.; Kim, M.-H.; Mun, Y.; Chun, J.; Ye, Y.; Hwang, J.; Ha, K.-S.; Roh, K. C.; Kang, K.; Yoon, S.; Lee, J. Facile synthesis of Nb_2O_5@carbon core-shell nanocrystals with controlled crystalline structure for high-power anodes in hybrid supercapacitors. *ACS Nano* **2015**, *9*, 7497−7505.

(27) Tao, Y.; Wei, Y.; Liu, Y.; Wang, J.; Qiao, W.; Ling, L.; Long, D. Kinetically-enhanced polysulfide redox reactions by Nb_2O_5 nanocrystals for high-rate lithium−sulfur battery. *Energy Environ. Sci.* **2016**, *9*, 3230−3239.

(28) Liu, Y.; Zhang, N.; Yu, C.; Jiao, L.; Chen, J. $MnFe_2O_4$@C nanofibers as high-performance anode for sodium-ion batteries. *Nano Lett.* **2016**, *16*, 3321−3328.

(29) Clark, S. J.; Segall, M. D.; Pickard, C. J.; Hasnip, P. J.; Probert, M. J.; Refson, K.; Payne, M. C. First principles methods using CASTEP. *Z. Krist-cryst. Mater.* **2005**, *220*, 567−570.

(30) Kamysbayev, V.; Filatov, A. S.; Hu, H.; Rui, X.; Lagunas, F.; Wang, D.; Klie, R. F.; Talapin, D. V. Covalent surface modifications and superconductivity of two-dimensional metal carbide MXenes. *Science* **2020**, *369*, 979−983.

(31) VahidMohammadi, A.; Rosen, J.; Gogotsi, Y. The world of two-dimensional carbides and nitrides (MXenes). *Science* **2021**, *372*, 6547.

(32) Purbayanto, M. A. K.; Nurfani, E.; Chichvarina, O.; Ding, J.; Rusydi, A.; Darma, Y. Oxygen vacancy enhancement promoting strong green emission through surface modification in ZnO thin film. *Appl. Surf. Sci.* **2018**, *462*, 466−470.

(33) Zhang, H.; Xin, X.; Liu, H.; Huang, H.; Chen, N.; Xie, Y.; Deng, W.; Guo, C.; Yang, W. Enhancing lithium adsorption and diffusion toward extraordinary lithium storage capability of free-standing $Ti_3C_2T_x$ MXene. *J. Phys. Chem. C* **2019**, *123*, 2792−2800.

(34) Xie, Y.; Zhang, H.; Huang, H.; Wang, Z.; Xu, Z.; Zhao, H.; Wang, Y.; Chen, N.; Yang, W. High-voltage asymmetric MXene-based on-chip micro-supercapacitors. *Nano Energy* **2020**, *74*, 104928.

(35) Wang, Z.; Xu, Z.; Huang, H.; Chu, X.; Xie, Y.; Xiong, D.; Yan, C.; Zhao, H.; Zhang, H.; Yang, W. Unraveling and regulating self-discharge behavior of $Ti_3C_2T_x$ MXene-based supercapacitors. *ACS Nano* **2020**, *14*, 4916−4924.

(36) Yi, S.; Wang, L.; Zhang, X.; Li, C.; Liu, W.; Wang, K.; Sun, X.; Xu, Y.; Yang, Z.; Cao, Y.; Sun, J.; Ma, Y. Cationic intermediates assisted self-assembly two-dimensional $Ti_3C_2T_x$/rGO hybrid nanoflakes for advanced lithium-ion capacitors. *Sci. Bull.* **2021**, *66*, 914−924.

(37) Wang, L.; Zhang, X.; Xu, Y. N.; Li, C.; Liu, W. J.; Yi, S.; Wang, K.; Sun, X. Z.; Wu, Z. S.; Ma, Y. W. Tetrabutylammonium-Intercalated 1T-MoS_2 Nanosheets with Expanded Interlayer Spacing Vertically Coupled on 2D Delaminated MXene for High-Performance Lithium-Ion Capacitors. *Adv. Funct. Mater.* **2021**, *31*, 2104286.

(38) Luo, D.; Zhang, Z.; Li, G.; Cheng, S.; Li, S.; Li, J.; Gao, R.; Li, M.; Sy, S.; Deng, Y. P.; Jiang, Y.; Zhu, Y.; Dou, H.; Hu, Y.; Yu, A.; Chen, Z. Revealing the rapid electrocatalytic behavior of ultrafine amorphous defective Nb_2O_{5-x} nanocluster toward superior Li-S performance. *ACS Nano* **2020**, *14*, 4849−4860.

(39) Gao, R.; Li, Z.; Zhang, X.; Zhang, J.; Hu, Z.; Liu, X. Carbon-dotted defective CoO with oxygen vacancies: a synergetic design of bifunctional cathode catalyst for Li−O_2 batteries. *ACS Catal.* **2016**, *6*, 400−406.

(40) Lu, S.; Wang, H.; Zhou, J.; Wu, X.; Qin, W. Atomic layer deposition of ZnO on carbon black as nanostructured anode materials for high-performance lithium-ion batteries. *Nanoscale* **2017**, *9*, 1184−1192.

(41) Zhou, T.; Zheng, Y.; Gao, H.; Min, S.; Li, S.; Liu, H. K.; Guo, Z. Surface engineering and design strategy for surface-amorphized TiO_2@graphene hybrids for high power Li-ion battery electrodes. *Adv. Sci.* **2015**, *2*, 1500027.

(42) Zheng, Y.; Zhou, T.; Zhao, X.; Pang, W. K.; Gao, H.; Li, S.; Zhou, Z.; Liu, H.; Guo, Z. Atomic interface engineering and electric-field effect in ultrathin Bi_2MoO_6 nanosheets for superior lithium ion storage. *Adv. Mater.* **2017**, *29*, 1700396.

(43) Stepniak, I.; Ciszewski, A. Grafting effect on the wetting and electrochemical performance of carbon cloth electrode and polypropylene separator in electric double layer capacitor. *J. Power Sources* **2010**, *195*, 5130−5137.

(44) Taberna, P. L.; Simon, P.; Fauvarque, J. F. Electrochemical characteristics and impedance spectroscopy studies of carbon-carbon supercapacitors. *J. Electrochem. Soc.* **2003**, *150*, A292−A300.

(45) Lou, S.; Cheng, X.; Zhao, Y.; Lushington, A.; Gao, J.; Li, Q.; Zuo, P.; Wang, B.; Gao, Y.; Ma, Y.; Du, C.; Yin, G.; Sun, X. Superior performance of ordered macroporous $TiNb_2O_7$ anodes for lithium ion batteries: Understanding from the structural and pseudocapacitive insights on achieving high rate capability. *Nano Energy* **2017**, *34*, 15−25.

(46) Wang, Y.; Chu, X.; Zhu, Z.; Xiong, D.; Zhang, H.; Yang, W. Dynamically evolving 2D supramolecular polyaniline nanosheets for long0stability flexible supercapacitors. *Chem. Eng. J.* **2021**, *423*, 130203.

https://doi.org/10.1021/acsaem.1c03680
ACS Appl. Energy Mater. XXXX, XXX, XXX−XXX